Materials Research Bulletin 107 (2018) 295–307

Contents lists available at ScienceDirect

Materials Research Bulletin

journal homepage: www.elsevier.com/locate/matresbu

SiO_2-TiO_2 doped with Er^{3+}/Yb^{3+}/Eu^{3+} photoluminescent material: A spectroscopy and structural study about potential application for improvement of the efficiency on solar cells

Juliana M.M. Buarque[a], Danilo Manzani[b], Sérgio Luis Scarpari[c], Marcelo Nalin[c], Sidney J.L. Ribeiro[c], Jennifer Esbenshade[d], Marco A. Schiavon[a], Jefferson L. Ferrari[a,e,*]

[a] Grupo de Pesquisa em Química de Materiais – (GPQM), Departamento de Ciências Naturais, Universidade Federal de São João Del Rei, Campus Dom Bosco, Praça Dom Helvécio, 74, 36301-160, São João Del Rei, MG, Brazil
[b] São Carlos Institute of Chemistry – IQSC, University of São Paulo – USP, CP 780, São Carlos, SP, Brazil
[c] Instituto de Química, UNESP, P.O. Box 355, 14800-970, Araraquara, SP, Brazil
[d] Department of Chemistry and Physics, University of Tennessee at Martin, Martin, TN, USA
[e] Desenvolvimento de Materiais Inorgânicos com Terras Raras – (DeMITeR), Instituto de Química – (IQ), Universidade Federal de Uberlândia – (UFU) Av. João Naves de Ávila, 2121, Bairro Santa Mônica, CEP: 38400-902, Uberlândia, MG, Brazil

ARTICLE INFO

Keywords:
Rare earths
Downconversion
Upconversion
Titanium dioxide
Solar cells

ABSTRACT

The various synthesis conditions to obtain a material based on SiO_2-TiO_2 co-doped with Er^{3+}/Yb^{3+}/Eu^{3+} were investigated, searching for those that present the greatest potential to improve the efficiency of solar cells. Conditions adjusted included heat-treatment temperatures, concentrations of matrix, and concentrations of dopants. Raman spectroscopy results demonstrated the effect of the annealing temperatures on the TiO_2 phase transition and the crystalline phase of the materials, which interfere with the photoluminescence of the materials. The band gap of the materials was evaluated by diffuse reflectance and it decreased due to the doping. The materials were able to absorb UV and IR energy and emit in the visible region, verified by the down conversion, up conversion and the double excitation of the materials. The results showed that the materials may be used as a strategy to use a greater portion of the solar spectrum, improving solar cell efficiency.

1. Introduction

With the technological development there has been an increase in energy demand [1] and many current energy sources come with high environmental cost. Thus, many studies have addressed the search for high performance alternative energy production devices [2]. Thus, there is great interest in alternative energy forms with good energy conversion efficiency and competitive costs, and dye-sensitized solar cells (DSSC) have proven to be an excellent alternative [3]. The manufacturing of DSSC does not require toxic materials and have a low cost. The conversion efficiency allows for an extension from the levels established by the Shockley equation. Their current efficiency is around 13%, increasing each year [4]. In the DSSC, the photoexcitation occurs on the dye; the dye absorbs a photon promoting their electrons from the highest occupied molecular orbital (HOMO) to the lowest unoccupied molecular orbital (LUMO). The injection of the electrons on the conduction band of the semiconductor occurs if its energy is lower than the LUMO [5]. The vacancies formed on the dye induce oxidation reactions that promote the generation of a current [6].

One way to optimize the DSSC is to increase the electron injection on the semiconductor. Alternatively, the materials could be doped in order to reduce the band gap [7]. Research on doped-TiO_2 solar cells demonstrate efficiency gains [8–11]. Another method to improve the efficiency of solar cells is to enhance the dye absorption [6]. Generally, the generation of the current flow is more effective when the dye absorptions occur at wavelengths located in the visible region of the electromagnetic spectrum, between 480 and 650 nm. However, considering that a large part of the solar radiation is ultraviolet (UV) and infrared (IR) light which is not able to promote the photoexcitation of the dye, the development of materials able to absorb energy at different wavelengths and emit in the visible region may promote an increase of the dye absorption. This strategy can change the useable wavelengths, utilizing more of the solar spectrum, thereby enhancing the efficiency of the solar cells [12–14].

* Corresponding author at: Desenvolvimento de Materiais Inorgânicos com Terras Raras (DeMITeR), Universidade Federal de Uberlândia, Instituto de Química – Bloco 1D, Av. João Naves de Ávila, 2121 – Santa Mônica, Uberlândia, MG, Brazil.
E-mail address: jeffersonferrari@ufu.br (J.L. Ferrari).

https://doi.org/10.1016/j.materresbull.2018.07.007
Received 23 May 2018; Received in revised form 5 July 2018; Accepted 5 July 2018
Available online 06 July 2018

The rare earth ions (RE^{3+}) promote the emergence of photoluminescent properties in systems that, before their incorporation, were not presenting these characteristics [15]. The europium ion (Eu^{3+}) has a characteristic absorption in the UV region and a strong visible emission, with red color, doing a downconversion mechanism [16–19]. The erbium ion (Er^{3+}) exhibits *up conversion* properties. It can absorb two or more photons with long wavelengths in the IR region and emit one photon with greater energy, in the visible region [20]. Er^{3+} also does a downconversion mechanism, absorbing a photon (980 nm) and after, emitting a photon with smaller energy (1150 nm). Due to the intense and extended emission, located in the telecommunications region, Er^{3+} is widely used in optical amplifiers [22,23]. The ytterbium ion (Yb^{3+}) has only two energy levels: $^2F_{7/2}$ and $^2F_{5/2}$ and does not present excited state absorption or *up conversion*. Moreover, their $^2F_{5/2}$ level is resonant with the $^4I_{11/2}$ level of the Er^{3+}. Thus, it is an erbium sensitizer [12,23].

Binary oxide systems are excellent matrices for RE^{3+} incorporation [23–25]. The variation of their composition significantly alters several properties of the materials, for example: refractive index, the solubility of the RE^{3+}, the crystallite sizes, the resistivity, the surface roughness, the thickness, and others [26,27]. The control of these properties allows for the tuning of the systems for different applications. A high refractive index is a basic condition for a good waveguide [28]. It is also important in solar cells. Their high value and the control of the surface roughness avoid losses by reflection. The analyses of the solubility of the RE^{3+} are essential to improve the photoluminescence properties and the life times of the excited state as they depend on the oxide ratio [29].

In optical devices, the use of materials containing SiO_2 favors adhesion at the interface between the fiber and amplifier, decreasing scattering losses [30]. The silica films have antireflective coating properties. This property can increase the solar cells efficiency. On the other hand, TiO_2 has excellent photocatalytic properties [31]. Both, SiO_2 and TiO_2, are nontoxic, are transparent over a wide region of the electromagnetic spectrum, have a low manufacturing costs, and good chemical and thermal stability. In light of these properties, the SiO_2-TiO_2 is a promising binary oxide system that presents excellent optical properties and has interested several researchers [32].

The goal of this work is to determine which parameters should be used to ensure the best synthesis conditions of the SiO_2-TiO_2 co-doped with $Er^{3+}/Yb^{3+}/Eu^{3+}$ material presenting the greatest potential for application to improve the efficiency of solar cells or that may be used in other high-tech devices. For this purpose, different materials were synthesized varying the ratio between the oxides, the percentages of the dopants and the temperature of heat treatment and their structural, optical and spectroscopic properties were studied. This research is working towards developing a more efficient DSSC.

2. Experimental details

2.1. Synthesis

The $Er^{3+}/Yb^{3+}/Eu^{3+}$ co-doped SiO_2-TiO_2 materials were synthetized via a sol-gel process. Materials with matrices containing $30Si^{4+}$:$70Ti^{4+}$ and $70Si^{4+}$:$30Ti^{4+}$ were analyzed. The molar concentration of $[Si^{4+} + Ti^{4+}]$ solution was kept at 0.445 mol.L^{-1} to calculate the molar ratio between Si^{4+}:Ti^{4+} ions. This relation was based on the synthesis previously reported by Ferrari et al. [33]. The percentage of dopants is related to the number of moles of $[Si^{4+} + Ti^{4+}]$. The concentration of Yb^{3+} was 1.2 mol% and Eu^{3+} was 2.0 mol%. The concentrations of Er^{3+} in the samples were 0.1, 1.0, 3.0 and 7.0 mol% with respect to the 0.445 mol L^{-1}.

Er_2O_3, Yb_2O_3 and Eu_2O_3 – Sigma Aldrich −99.99% were diluted in separate containers of hydrochloric acid solution followed by solvent extraction using anhydrous ethanol to obtain the RE^{3+} ethanol solution with a pH around 5.8. The RE^{3+} ethanol solutions were standardized using complexometric titration with EDTA (ethylene diamine tetra acetic acid – 0.01 mol L^{-1}). In the synthesis of materials reported here the tetraethylorthosilicate – TEOS (Sigma Aldrich, 98%) and tetra isopropyl orthotitanate – TTIP (Merck, 97%) were used as precursors of Si and Ti, respectively. Two solutions were prepared, each one containing 20 mL. The first one contained anhydrous ethanol, TEOS and 0.27 mol L^{-1} hydrochloric acid to control the hydrolysis process. The molar ratio between [TEOS] and [HCl] was [1] and [0.007], respectively. The second one contained anhydrous ethanol, TTIP and the solutions of RE^{3+}. Both solutions were kept under stirring at room temperature for 10 min and then were mixed. The resulting solution was kept under stirring for 15 min. The *sol* obtained were kept in an oven during 24 h at 60 °C to obtain the xerogels. The xerogels obtained were ground in an agate mortar and the powers obtained were heat-treated at 700, 800, 900 and 1000 °C for 5 h. To obtain the final material in powder form, the heating rate was kept at 1 °C/minute. However, the heat treatment was divided into 3 steps. The first step, the temperature was started at room temperature and heated up to 150 °C for 1 h. The second step, the temperature was increased to 275 °C and kept at that temperature for one more hour. Finally, the temperature was increased to the final temperature for the heat treatment.

2.2. Characterization

2.2.1. Raman spectroscopy

The Raman spectrum in the 50 and 700 cm^{-1} region were obtained by a Raman LabRam-HR spectrophotometer, using a 632.81 nm laser as the excitation source, 1800 lines/nm grating, LWD 50Xobjective lens and a laser spot diameter of approximately 1 μm on the surface of the sample.

2.2.2. Diffuse reflectance spectroscopy

The absorptions in the UV–vis region of the materials were collected though the diffuse reflectance spectroscopy, in the range of wavelengths between 200–750 nm. The apparatus used was a Shimadzu UV-2401 PC instrument. This technique was also used to obtain the band gap of the materials.

2.2.3. Photoluminescense analyses

All the photoluminescence results were obtained at room temperature on SPEXF2121/Jobin-Yvon Fluorolog equipment. For the downconversion analyses, a Xe 450 W lamp was used as excitation source. The materials were excited at 394 and 463 nm and the emission spectra were collected in the range 500–700 nm. The excitation and emission slits were 5 nm and 2 nm, respectively, and the integration time was 0.1 s. The lifetime curves were collected using a pulsed lamp. The excitation wavelength used was 394 and 463 nm and the emission wavelength used was the maximum observed for the emission assigned to the $^5D_0 \rightarrow {}^7F_2$ transition emission band. For emissions by up conversion, the 980 nm laser was used as an excitation source, changing the power pump from 100 to 4000 mW. The emission slit was fixed at 10 nm. The performance of the photoluminescence materials in front of a double excitation was available. Photons in the UV (394/463 nm) and the IR (980 nm) regions were used simultaneously to excite the materials, and their emissions were collected. The parameters of the UV excitation were the same as reported before – and the power pump for the IR excitation laser with wavelength of 980 nm laser was fixed at 3200 mW. The emissions slit were 2 nm and the results were collected in the 500–700 nm range. The infrared emissions were collected at 1400–1700 nm wavelength. A 980 nm diode laser was used as an excitation source and the power pump was changed from 100 to 4000 mW.

3. Results and discussion

The crystalline phase of most of the materials was determined by Raman spectroscopy and the results are presented in Fig. 1. The samples

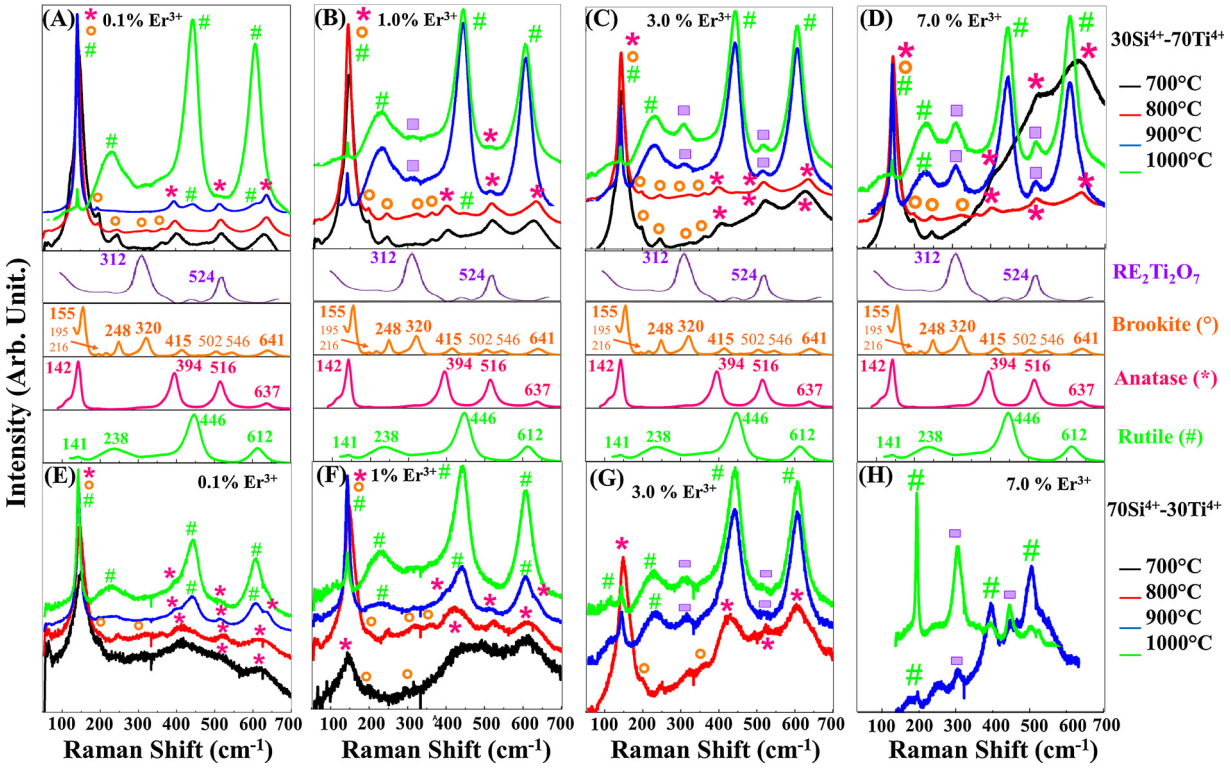

Fig. 1. Raman Spectra obtained of the samples based on $30Si^{4+}$-$70Ti^{4+}$ heat-treated at different temperatures and co-doped with x mol% of Er^{3+}/1.2 mol% of Yb^{3+}/ 2.0 mol% of Eu^{3+} (A) 0.1 Er^{3+}, (B) 1.0 Er^{3+}, (C) 3.0 Er^{3+}, (D) 7.0 mol% of Er^{3+}, and the samples based on $70Si^{4+}$-$30Ti^{4+}$ heat-treated at different temperatures and co-doped with x mol% of Er^{3+}/1.2 mol% of Yb^{3+}/2.0 mol% of Eu^{3+} (A) 0.1 Er^{3+}, (B) 1.0 Er^{3+}, (C) 3.0 Er^{3+}, (D) 7.0 mol% of Er^{3+}.

Table 1
Phase composition of the materials based on SiO_2-TiO_2 : x Er^{3+} : 1.2 mol% of Yb^{3+} : 2.0 mol% of Eu^{3+} where x = 0.1, 1.0, 3.0 and 7.0 mol%, heat-treated at 700, 800, 900 and 1000 °C prepared by the sol-gel process.

Percentage of phase of the materials based on $30Si^{4+}$ - $70Ti^{4+}$

Temp. (°C)	0.1 mol% of Er^{3+}				1.0 mol% of Er^{3+}				3.0 mol% of Er^{3+}				7.0 mol% of Er^{3+}			
	A	B	R	T	A	B	R	T	A	B	R	T	A	B	R	T
700 °C	36.45	63.55	0	0	50.55	49.45	0	0	66.52	33.48	0	0	83.40	16.60	0	0
800 °C	58.68	41.32	0	0	47.46	33.89	18.65	0	54.12	24.31	21.56	0	51.12	20.80	28.08	0
900 °C	39.70	21.46	38.84	0	0	0	88.34	11.65	0	0	83.57	16.73	0	0	77.84	22.16
1000 °C	0	0	100	0	0	0	88.49	11.51	0	0	83.70	16.30	0	0	76.27	23.73

Percentage of phase of the materials based on $70Si^{4+}$ - $30Ti^{4+}$

Temp. (°C)	0.1 mol% of Er^{3+}				1.0 mol% of Er^{3+}				3.0 mol% of Er^{3+}				7.0 mol% of Er^{3+}			
	A	B	R	T	A	B	R	T	A	B	R	T	A	B	R	T
700 °C	–	–	–	–	–	–	–	–	–	–	–	–	–	–	–	–
800 °C	30.71	37.88	31.42	0	42.38	30.03	27.59	0	56.66	23.42	19.91	0	–	–	–	–
900 °C	19.71	22.62	57.66	0	19.96	0	80.04	0	0	0	73.87	26.13	0	0	82.26	17.74
1000 °C	17.66	0	82.34	0	0	0	100	0	0	0	71.34	28.64	0	0	19.79	80.21

A; Anatase crystalline phase B: Brookite crystalline phase R: Rutile crystalline phase T: Titanate crystalline phase.
– : It was not possible to determine the phase percentage.

based on $70Si^{3+}$-$30Ti^{3+}$, heat treated at lower temperatures and containing a higher concentration of Er^{3+}, were the only that presented luminescence and their modes of vibration were covered.

Among the polymorphs of TiO_2, the rutile is the most thermodynamically stable [34]. The anatase (tetragonal - D_{4h}-I_{41}/point group), has six Raman active modes of vibration (A_{1g} + $2B_{1g}$ + $3E_g$) that present in 144 (E_g), 197 (B_{1g}), 399 (B_{1g}), 513 (A_{1g}), 519 (B_{1g}) and 639 cm^{-1} (E_g) [35]. The vibrational modes of rutile (tetragonal - D_{4h}-P_{42}/point group) are positioned at 144 (B_{1g}), 239 (multi-photons process), 448 (E_g) and 612 cm^{-1} (A_{1g}) [26]. The unit cell of brookite (Orthorhombic – D_{2h}-P_{bca}/point group) is large and has low symmetry; consequently, its Raman spectrum is complicated. The brookite phase has 60 vibrational modes, of which 36 are active in Raman: $9A_{1g}$ (125, 155, 194, 247, 324, 412, 492, 545 and 636 cm^{-1}), $9B_{1g}$ (133, 213, 322, 425 and 501 cm^{-1}), $9B_{2g}$ (254, 329, 366, 395, 460 and 583 cm^{-1}) and $9B_{3g}$ (172, 287, 452, 545 and 618 cm^{-1}) but their intensities are not very strong [36,37].

The materials present an amorphous phase of SiO_2 and a crystalline phase of TiO_2. In all samples, there is a coexistence of two or more crystalline phases of TiO_2. Some vibrational modes are associated with

the specific phase. The 197 cm^{-1} mode is characteristic to brookite and the mode around ~516 cm^{-1} happens only in the anatase phase. Rutile has a unique mode at ~443 cm^{-1}. Therefore, it is possible to estimate the quantity of each crystalline phase present in the samples, according to the following Eqs. (1–3) [38]:

$$A_{\%\,(Int)} = \frac{I_A}{I_R + I_A + I_B} \quad (1)$$

$$B_{\%\,(Int)} = \frac{I_B}{I_R + I_A + I_B} \quad (2)$$

$$R_{\%\,(Int)} = \frac{I_R}{I_R + I_A + I_B} \quad (3)$$

Where $A_{\%}$, $B_{\%}$ and $R_{\%}$ are the percentages of the anatase, brookite and rutile phases respectively and I_A, I_B and I_R are the intensity of the vibrational phase-specific modes of each phase. The amounts of the phases are present in Table 1.

At lower temperatures, the predominant phases are anatase and brookite. However, increasing the temperature of the heat treatment favors the formation of rutile phase. Some authors have reported that the formation of the rutile phase starts at relatively low temperatures (300 °C for the pure TiO_2) [39]. However, the results obtained show the formation of rutile phase only at 800 °C. This indicates that the presence of Si^{4+} and the dopants stabilize the metastable phases. The metastable phases are more suitable for the photoluminescence properties of the material and more active for photo catalysis. Their presence at higher temperatures is attractive, decreasing the defects and suppressor groups of the photoluminescence, for example the -OH group. At temperatures above 900 °C, the formation of the titanate phase is observed.

The Raman spectroscopy results also provide information about the size of the nanometric particles. In vibrational transitions, the wave number changes according to the force constant ($K^{1/2}$) [35]. The interatomic distance is indirectly proportional to the force constant. Thus, the smaller the interatomic distance, the greater the force constant and, consequently, the modes of vibration occur at higher wave numbers. Table 2 shows the position of the E_g mode and the value of the full width at half maximum (*FWHM*). Increasing the heat-treatment temperature, the position of the band assigned to the E_g mode and the *FWHM* decrease considerably. The coalescence of the crystallites is favored for higher temperatures. Larger crystallites have a weaker force constant and their vibrational modes occur at lower wave numbers. On the other hand, the presence of defects in the material promotes a break in the symmetry of the crystal, provoking the enlargement of the *FWHM* of these modes. At higher temperatures, the defects become smaller and the same occurs with bandwidth. The samples containing a higher concentration of Si^{4+} have smaller crystallites and larger bands.

Fig. 2 exhibits the reflectance spectra of the materials. These provide the details of the interaction between the samples and the electromagnetic radiation. The occurrence of some bands with wavelengths in the 450–700 nm regions is due to the energy absorption by the RE^{3+}. These bands are identified according to the following transitions: $^4I_{15/2} \rightarrow {}^4F_{9/2}$ (~654.5 nm), $^4I_{15/2} \rightarrow {}^4S_{3/2}$ (~ 545.15 nm), $^4I_{15/2} \rightarrow {}^2H_{11/2}$ (~ 521.5 nm), $^4I_{15/2} \rightarrow {}^4F_{7/2}$ (~ 488.3 nm) and $^4I_{15/2} \rightarrow {}^4F_{5/2}$ (~ 452.8 nm) – associated with the Er^{3+} [40]- and $^7F_0 \rightarrow {}^5D_2$ (~ 464 nm) and $^7F_0 \rightarrow {}^5L_6$ (~394 nm) – related to the Eu^{3+} [41]. The intensity of these bands increase as a function of Er^{3+} concentration in the system, as shown in Fig. 2(A).

The reflectance of the material is almost null at short wavelengths up to 350 nm, which means that they absorb these radiations. At wavelengths greater than 420 nm, the materials present a maximum reflectance. The absorption edge occurs in the region between 350–420 nm. According to Fig. 2(B), the absorption edge of the materials moves to higher wavelengths as a function of heat-treatment temperature. This effect may be assigned to the crystalline phase changing in the materials. Comparing the samples treated at the same temperature and has the same RE^{3+} concentration, the same occurs with the absorption edge when increasing the Ti^{4+} concentrations in the matrices.

The edge present in the spectrum is due to the energy absorption of the matrix, which provoke the promotion of the electrons from the valence band to the conduction band of the TiO_2. The Kubelka-Munk function relates the absorption (K) and the scattering coefficient of light (S) per wavelength, according Eq. (4) [35]. Where R_α is the reflectance of the material in each wavelength and *F(Rα)* is a function of Kubelka-Munk.

$$F(R) = \frac{K}{S} = \frac{(1-R)^2}{2R} \quad (4)$$

In theory, the anatase phase presents an indirect band gap whereas the band gap of rutile and brookite are associated with a direct transition [38]. However, the RE^{3+} incorporation creates acceptor/donor electron states. For this reason, independent of the crystalline phase of the materials, the band gap of the materials was calculated indirectly from plotting a graph of $[F\ (R_\alpha)h\nu]^{1/2}$ vs $h\nu$ and performing a linear adjustment, as shown in Fig. 2(C). The band gap values obtained for all materials are presented in Table 3.

Table 2
The position and FWHM of the E_g mode of the samples based on SiO_2-TiO_2: $2Eu^{3+}$: $1.2Yb^{3+}$: x Er^{3+} (x = 0.1. 1.0. 3.0 and 7.0 mol% heat-treated at 700. 800. 900 and 1000 °C prepared by the sol-gel process.

Samples based on $30Si^{4+}$ - $70Ti^{4+}$								
Temp. (°C)	0.1 mol% of Er^{3+}		1.0 mol% of Er^{3+}		3.0 mol% of Er^{3+}		7.0 mol% of Er^{3+}	
	E_g mode	FWHM	E_g mode	FWHM	E_g mode	FWHM	E_g mode	FWHM
700	146.26	27.00	146.26	29.31	146.26	29.20	145.94	27.88
800	143.39	16.09	144.02	20.22	144.02	19.50	143.03	19.38
900	142.12	9.70	141.80	8.44	142.11	9.66	142.11	9.57
1000	142.11	4.31	142.11	5.53	141.79	–	141.79	–
Samples based on $70Si^{4+}$ - $30Ti^{4+}$								
Temp. (°C)	0.1 mol% of Er^{3+}		1.0 mol% of Er^{3+}		3.0 mol% of Er^{3+}		7.0 mol% of Er^{3+}	
	E_g mode	FWHM	E_g mode	FWHM	E_g mode	FWHM	E_g mode	FWHM
700	150.75	40.96	142.75	42.32	–	–	–	–
800	145.38	29.13	148.17	30.42	148.17	37.65	–	–
900	143.71	12.44	143.39	12.87	143.07	26.74	144.67	–
1000	142.75	10.29	143.07	11.48	143.71	13.90	141.16	9.38

FWHM: Full width at half maximum.

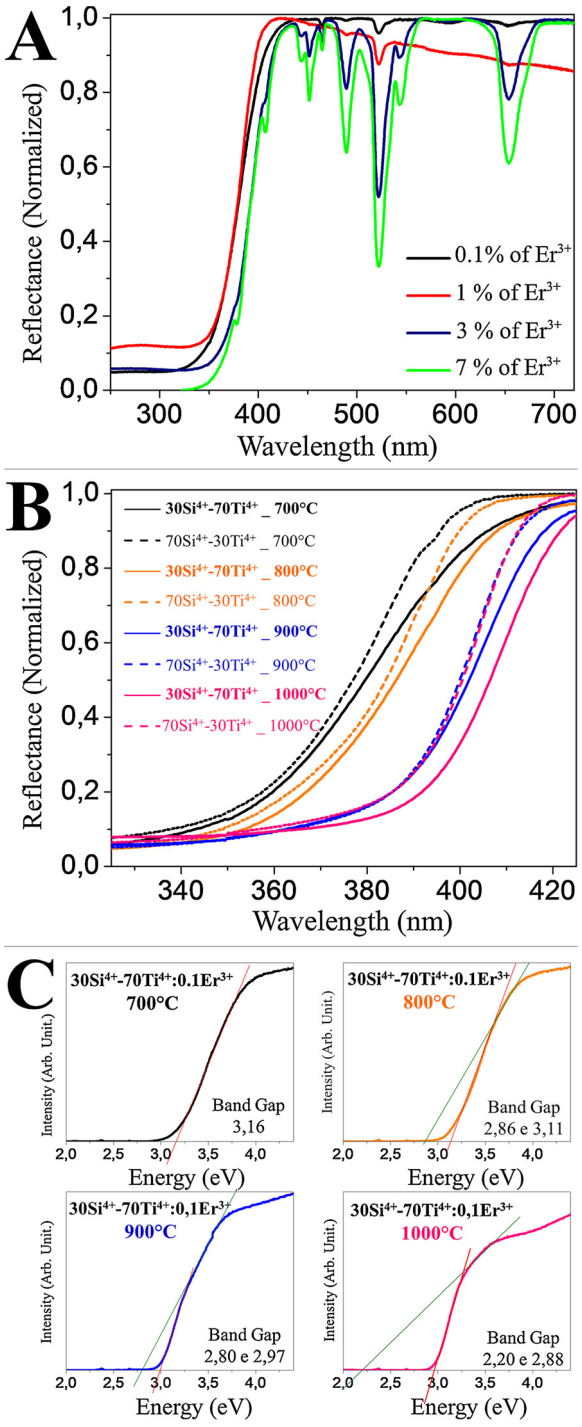

Fig. 2. (A) Diffuse Reflectance spectra of the samples based on $30Si^{4+}$-$70Ti^{4+}$ co-doped x mol% of Er^{3+}/1.2 mol% of Yb^{3+}/2.0 mol% of Eu^{3+} heat-treated at 700 °C where x = 0.1, 1.0, 3.0 and 7.0 mol% of Er^{3+}. (B) Diffuse Reflectance spectra of different matrices co-doped with 0.1 mol% of Er^{3+}/1.2 mol% of Yb^{3+}/2.0 mol% of Eu^{3+} and annealing temperatures. (C) The Indirectly Band Gap of the materials based on $30Si^{4+}$-$70Ti^{4+}$:0.1 mol% of Er^{3+}/1.2 mol% of Yb^{3+}/2.0 mol% of Eu^{3+}.

The band gap values depend on the crystalline phase of the materials. The values reported in the literature for the band gaps of pure anatase, brookite and rutile phases are 3.21, 3.13 and 3.0 *eV*, respectively [42]. As expected, the extrinsic conduction obtained though the doping of semiconductors reduces the distance between the bands of valence and conduction, provoking a decrease in the band gap. With the increase of heat-treatment temperature, the formation of the rutile phase is favored, and the band gap decreases. Some materials present two different band gap values, indicating the presence of two or more crystalline phases. These results are in concordance with the Raman results.

To check the downconversion properties of the materials two-excitation wavelengths (394 and 463 nm) an analysis was performed and the results are presented in Fig. 3. The materials containing Eu^{3+} can absorb energy in the UV–vis region promoting the following transition states: $^7F_0 \rightarrow {}^5L_6$ (~394 nm), $^7F_1 \rightarrow {}^5L_7$ (~400 nm), $^7F_0 \rightarrow {}^5D_2$ (~463 nm), $^7F_0 \rightarrow {}^5D_1$ (~525 nm), $^7F_1 \rightarrow {}^5D_1$ (~532 nm) [21,22,42]. All samples presented photoluminescence, although their intensities of emission varied. There is a loss of part of the absorbed energy by non-radiative emission processes and when the $^5D_0$ state is populated, the radiative emission occurs through the intra-configurational 4f-4f transitions. These emissions refer to the Eu^{3+} transitions: $^5D_0 \rightarrow {}^7F_0$ (~578 nm), $^5D_0 \rightarrow {}^7F_1$ (587–594 nm), $^5D_0 \rightarrow {}^7F_2$ (611–620 nm), $^5D_0 \rightarrow {}^7F_3$ (648–652 nm) e $^5D_0 \rightarrow {}^7F_4$ (685–701 nm) and it is possible to observe them in the emission spectrum [17,19]. Some bands assigned to the Er^{3+} transitions: $^2H_{11/2} \rightarrow {}^4I_{15/2}$ (~524 nm) e $^4S_{3/2} \rightarrow {}^4I_{15/2}$ (~545 nm) are also present [12]. The intensity of the Er^{3+} bands do not change and occur with intensity on the order to 10^4. Meanwhile, the Eu^{3+} emissions decrease dramatically with increasing heat-treatment temperature, whatever the composition of the systems, as exemplified at Fig. 3 [I – (A), (B) and II – I, (F)].

In addition to the intense red emission of the Eu^{3+}, another advantage is their application as a structural probe. The crystalline field does not interfere with the intensity of the $^5D_0 \rightarrow {}^7F_1$ transition once the nature of its dipole is magnetic [43,44]. Unlike this, the interaction between the electromagnetic radiation and the $^5D_0 \rightarrow {}^7F_2$ transition has an electric nature and is hypersensitive to the environment [45,46]. It is forbidden by parity and becomes permitted when the chemical environment is distorted or when the Eu^{3+} is not located at an inversion center. If this occurs, the transition is not observed [18,47]. Based on this, if the RE^{3+} are located in sites with high or low symmetry, the ratio between the integral areas of $^5D_0 \rightarrow {}^7F_2$ and $^5D_0 \rightarrow {}^7F_1$ transitions was calculated [48].

The values of the asymmetry are shown in Table 4. They need to be analyzed in conjunction with the other results. Higher values of this proportion indicate that the local symmetry around the Eu^{3+} is smaller. Comparing the polymorphs of TiO_2, the metastable phases exhibit lower symmetry than the rutile phase, which has a center of inversion symmetry. As shown in the Raman results, at 700 and 800 °C, the anatase and brookite are present in all of the samples while at 900 and 1000 °C, the predominant phase is rutile; consequentially the values of the asymmetric ratio diminish at higher temperatures. The formation of the rutile phase explains the considerable reduction of the photoluminescence when the heat-treatment temperature increases. Despite the decline of the photoluminescence, it does not disappear. It indicates that the incorporation of RE^{3+} distort the crystallites, which is expected due to the great difference between the ionic radii – Eu^{3+} (0.947 Å), Ti^{4+} (0.605 Å) for coordination number equal to six [28,34] and Si^{4+} (0.420 Å) for coordination number equal to four [49]. The results show that the Eu^{3+} responsible for the emissions is located in the TiO_2. Part of the ions may also be located in the vacancies or at the surface of the material, but the energy absorbed by them are quickly lost by a non-radiative emission process. The samples with a higher percentage of Ti^{4+} ions present more intense emissions. At higher Si^{4+} concentrations, a greater deal of RE^{3+} is located at defects, vacancies or on the surface, hurting the photoluminescence properties.

The $^5D_0 \rightarrow {}^7F_0$ transition of the Eu^{3+} provides information about the local structure of the Eu^{3+}. In this transition, both states are non-degenerate (J = 0) [50], meaning that their degeneracy is equal to one and the Stark Effect is not pronounced [51]. The widths of the band attributed to the $^5D_0 \rightarrow {}^7F_0$ transition were calculated and the results are shown in Table 5. This band becomes wider with the higher dopant concentration and with an increase in the heat-treatment temperature.

Table 3
Band Gap values calculated using Kubelka-Munk Methods for the samples based on SiO_2-TiO_2 co-doped with x mol% of Er^{3+}/ 1.2 mol% of Yb^{3+}/ 2.0 mol% of Eu^3 where x = 0.1, 1, 3 and 7 mol% and the matrices concentrations are $30Si^{4+}$ -$70Ti^{4+}$ or $70Si^{4+}$ -$30Ti^{4+}$ heat-treated at 700, 800, 900 and 1000 °C prepared by the sol-gel process.

The bandgap of the samples based on $30Si^{4+}$ - $70Ti^{4+}$ (eV)				
Temp. (°C)	0.1 mol% of Er^{3+}	1.0 mol% of Er^{3+}	3.0 mol% of Er^{3+}	7.0 mol % of Er^{3+}
700	3.19	3.12	3.08	3.11
800	3.15 / 2.86	3.10 / 3.01	3.04 / 3.02	3.04
900	3.02 / 2.84	2.99 / 2.88	2.98 / 2.66	2.99
1000	2.95 / 2.60	2.99 / 2.51	2.83 / 2.55	2.99
The bandgap of the samples based on $70Si^{4+}$ - $30Ti^{4+}$ (eV)				
Temp. (°C)	0.1 mol% of Er^{3+}	1.0 mol% of Er^{3+}	3.0 mol% of Er^{3+}	7.0 mol% of Er^{3+}
700	3.18	2.98	3.09	3.19 / 2.88
800	2.99 / 2.94	2.98 / 2.93	2.92 / 2.62	3.02 / 2.62
900	2.98 / 2.83	2.90 / 2.55	2.92 / 2.59	2.94 / 2.73
1000	2.93	2.90 / 2.50	2.95 / 2.47	2.94 / 2.23

The enlargement of the $^5D_0 \rightarrow {}^7F_0$ band when the annealing temperature increases suggests the presence of Eu^{3+} in more than one symmetry site. On the other hand, the offset of the modes of vibration at smaller wavenumbers and the narrowing of the FWHM in the Raman results, indicate the increase in the crystallite size and a smaller break in the crystallinity of the materials. So, greater amounts of RE^{3+} are located in vacancies.

Fig. 3 [I – I, (D) and II – (G), (H)] shows that when the increasing the dopant concentration, the photoluminescence intensity of the band assigned to the $^5D_0 \rightarrow {}^7F_2$ transition decreases drastically. This is due to the cross relation process where the distance between the RE^{3+} decreases with the presence of a large amount immediately allowing the absorption of the energy emitted by one RE^{3+} by its neighbor. Another possible explanation is the difficulty of incorporating all the RE^{3+} inside the crystalline structure, allowing them to be located in the defects or in the surface of the materials. Thus, they lose their energy by a non-radiative emission process.

The samples based on $30Si^{4+}$-$70Ti^{4+}$ doped with $0.1Er^{3+}$/ $1.2Yb^{3+}$/$2.0Eu^{3+}$ exhibited the highest emission intensity, shown by their lifetime measurements. The excitation wavelength was 394 nm or 463 nm and the emission wavelength was fixed on the maximum intensity correspondent of each sample. Using an exponential adjustment of the first order established the values of the lifetimes, as shown in Fig. 4(A).

Fig. 4(B) correlates the lifetime of the materials with the different annealing temperatures. As expected, their values decreased with the increasing of the temperature. The lifetime values of the samples treated at 700 or 800 °C are larger than the values reported in the literature for TiO_2:Eu^{3+} (0.55 ms) [51].

The Er^{3+} presented the up conversion phenomenon, thus the materials may also exhibit this property. Fig. 5(A) shows the emission spectra in the visible region of the materials under excitation at 980 nm laser pumping and ranging the power from 200 to 4000 mW. This phenomenon occurred in all samples. Increasing the laser power pump, the emission intensity also increased, according to Fig. 5(A). The presence of three large bands was noted, associated with transitions between Er^{3+} states: $^2H_{11/2} \rightarrow {}^4I_{15/2}$ (~530 nm), $^4S_{3/2} \rightarrow {}^4I_{15/2}$ (~551 nm) e $^4F_{9/2} \rightarrow {}^4I_{15/2}$ (~663 nm) [11].

The laser power (P) and the number of photons involved in the excitation process (n) influenced the photoluminescent properties, according to Equation 5. The emission intensity (I_f) may be obtained through the areas of the emission curves of the transitions $^2H_{11/2} \rightarrow {}^4I_{15/2}$ + $^4S_{3/2} \rightarrow {}^4I_{15/2}$ and $^4F_{9/2} \rightarrow {}^4I_{15/2}$ [52].

$$I_f \propto P^n \quad (5)$$

The number of photons involved in the up conversion process corresponds to the angular coefficient according to Fig. 5(B) and the values related to the excitation photons listed in Table 6.

The slope values are close to 2 indicating that two photons are involved in the process. The first possible mechanism occurs through the energy transfer between the Yb^{3+} and Er^{3+} ions (Mechanism 1 – E.T. at Fig. 6). The Yb^{3+} ion presents the $^2F_{7/2}$ and $^2F_{5/2}$ that can be populated and acts as a mains energy level to the up conversion mechanism in this specific case. For this reason, it is possible to use it like a sensitizer in systems that demand an energy donator. The $^2F_{5/2}$ level of Yb^{3+} is resonant with the $^4I_{11/2}$ level of the Er^{3+}. In addition, the sections of absorption shocks of Yb^{3+} is 10 times more efficient than the Er^{3+} ion [53]. Through the absorption of a 980 nm pumping laser, the promotion of the electrons occurs from the ground state ($^2F_{7/2}$) to the excited state ($^2F_{5/2}$) of the Yb^{3+}. Then, the energy transfer happens inducting the $^4I_{15/2} \rightarrow {}^4I_{11/2}$ transition. Another Yb^{3+} absorbs a second photon and transfers the energy to the same Er^{3+}, encouraging the electron transition from the $^4I_{11/2}$ state to $^4F_{7/2}$ state. Part of this absorbed energy is lost by non-radiative processes allowing the occupation of $^2H_{11/2}$, $^4S_{3/2}$ or $^4F_{9/2}$ states. Then, an intense green emission may be observed through the transitions $^2H_{11/2} \rightarrow {}^4I_{15/2}$ (~530 nm) or $^4S_{3/2} \rightarrow {}^4I_{15/2}$ (~551 nm). The red emission is induced by the $^4F_{9/2} \rightarrow {}^4I_{15/2}$ transition.

Another possible mechanism occurs similarly, but without the energy transfer. The excitation happens by the absorption of an excited state (Mechanism 2 – ESA. in Fig. 6). The Er^{3+} ion absorbs a 980 nm pumping photon, promoting their electrons from the fundamental energy state ($^4I_{15/2}$) to the excited state ($^4I_{11/2}$). Then, the same ion absorbs another photon stimulating the occupation of the $^4F_{7/2}$ state. After some non-radiative emissions, the transitions $^2H_{11/2} \rightarrow {}^4I_{15/2}$, $^4S_{3/2} \rightarrow {}^4I_{15/2}$ or $^4F_{9/2} \rightarrow {}^4I_{15/2}$ occur.

A third possible mechanism (Mechanism 3 in Fig. 6) occurs if part of the energy absorbed after the first pumping laser is lost by non-radiative processes allowing the occupation of the $^4I_{13/2}$ state. Then, the absorption of a second photon, via ESA or by Energy Transfer promotes the electrons to the $^4S_{3/2}$ state. In this mechanism, only the emissions at about 551 nm and 657 nm occur.

According to Fig. 5 I and (D), some samples present a band located at 620 nm. It refers to the $^5D_0 \rightarrow {}^7F_2$ transition of the Eu^{3+}. The Eu^{3+} excitation by the absorption of a 980 nm photon is not possible once there are not states with this energy. A possible explanation is the occupation of $^5D_1$ state of the Eu^{3+} through the loss of part of the energy of $^4F_{7/2}$ state by a non-radiative process. Fig. 7 shows this likely mechanism.

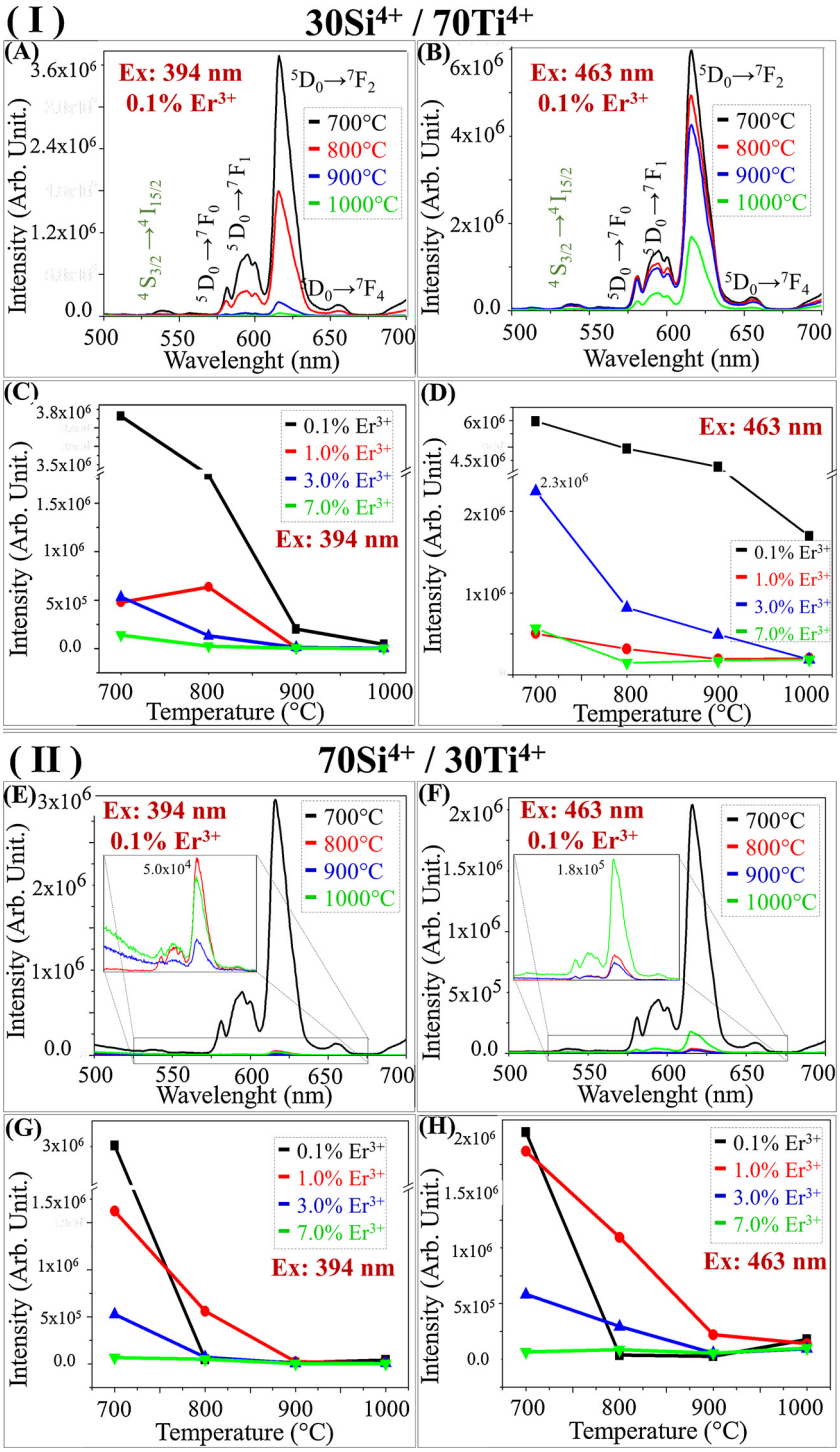

Fig. 3. Emission spectra of the samples based on [I] $30Si^{4+}$-$70Ti^{4+}$ and [II] $70Si^{4+}$-$30Ti^{4+}$. The results on the graphs (A), (B), (E) and (F) are from the samples co-doped with 0.1 mol% of Er^{3+}/1.2 mol% of Yb^{3+}/2.0 mol% of Eu^{3+} and treated at different temperatures under excitation at 394 nm or 463 nm. The graphs (C), (D), (G) and (H) exhibit a comparison of the emission intensity of the $^5D_0 \rightarrow {}^7F_2$ transition of the samples doped with different RE^{3+} concentrations under excitation at 394 nm or 463 nm.

The chromaticity diagrams give information about of the colors emitted through the up conversion process (Fig. 8). Their position close to the edge of the diagram suggests that the colors emitted by the materials are pure. The changing of the laser power pump changes the color emitted by the materials. Using low laser power, the emissions tend to be red. With the increase of the laser potency, the emissions are dislocated to smaller wavelengths and they become green in the higher powers of the laser.

The materials were submitted to a double excitation to simulate a circumstance closer to the solar excitation and investigate how they behave. An excitation beam in the UV region (394 or 463 nm) and another in the IR region (980 nm) was used.

The results of all the samples show emission bands assigned to the f-f transitions of Eu^{3+} and Er^{3+}, no matter the heat treatment temperature and the concentration of the dopant. Fig. 9(A) and (B) show the emission results obtained for the samples based on $30Si^{4+}$ -$70Ti^{4+}$

Table 4
Asymmetric ratio of the samples based on SiO_2-TiO_2: 2.0 mol% of Eu^{3+}: 1.2 mol% of Yb^{3+}: x mol% of Er^{3+} (x = 0.1. 1.0. 3.0 and 7.0 mol% heat-treated at 700. 800. 900 and 1000 °C prepared by the sol-gel process.

Ratio of the areas of the emission bands $^5D_0 \rightarrow {}^7F_2/{}^5D_0 \rightarrow {}^7F_1$ of the samples based on $30Si^{4+}$ - $70Ti^{4+}$								
Temp. (°C)	0.1 mol% of Er^{3+}		1.0 mol% of Er^{3+}		3.0 mol% of Er^{3+}		7.0 mols% of Er^{3+}	
	Excitation wavelength							
	394	463	394	463	394	463	394	463
700	3.76	4.00	3.95	4.27	3.28	4.08	3.28	3.77
800	4.31	4.19	4.22	3.83	3.28	3.55	2.43	3.20
900	4.01	4.10	1.44	3.46	–	3.45	1.71	3.17
1000	3.08	3.95	2.51	3.87	2.96	3.87	2.37	3.82
Ratio of the areas of the emission bands $^5D_0 \rightarrow {}^7F_2/{}^5D_0 \rightarrow {}^7F_1$ of the samples based on $70Si^{4+}$ - $30Ti^{4+}$								
Temp. (°C)	0.1 mol% of Er^{3+}		1.0 mol% of Er^{3+}		3.0 mol% of Er^{3+}		7.0 mol% of Er^{3+}	
	Excitation wavelength (nm)							
	394	463	394	463	394	463	394	463
700	3.66	4.30	3.96	4.28	3.22	3.55	1.96	1.93
800	4.21	4.77	4.20	4.65	3.39	4.02	2.90	3.15
900	2.56	3.75	2.84	4.19	1..54	2.87	1.91	4.68
1000	2.99	3.90	3.23	4.16	2.32	3.98	3.04	4.59

co-doped with 0.1 Er^{3+}/1.2 Yb^{3+}/2.0 Eu^{3+} heat-treated at (A) 700 and (B) 1000 °C. The emission located in the green region (between 500–574 nm), originating from the Er^{3+} transitions are more intense from the double excitation than the simple UV excitation. This agrees with the previous results, since the samples present the up conversion phenomenon. The percentage of green emission gain is higher in the samples with lower losses via non-radiative processes. The ratio between the green emission area of the samples excited by simple (394 nm) and double (394 and 980 nm) beams is 2.91, 1.04, 53.11 and 30.49 for systems heat-treated at 700, 800, 900 and 1000 °C, respectively. At lower temperatures, the disorder of the materials is highly compromised to the up conversion which is why the green emission gain is moderate. In contrast, the thermal energy supplied by the heat-treatment promotes the reduction of the photoluminescence suppressor groups, like −OH and the structure defects, causing a huge increase in the emission through double excitation. Other factors need to be consider, for example, the crystalline phase of the materials and the percentage of dopants, which cause losses by cross relation.

A comparison between the emission of the samples based on $30Si^{4+}$-$70Ti^{4+}$ and $70Si^{4+}$-$30Ti^{4+}$ are in the histograms in Fig. 9(C). The materials containing a higher percentage of Si^{4+} have lower emission intensity once the incorporation of RE^{3+} in the TiO_2 is cumbersome. In the samples with the other matrix ratios, the green emission area increases with the excitation by two different wavelengths at

Table 5
Width of the band assign to $^5D_0 \rightarrow {}^7F_0$ ratio of the samples based on SiO_2-TiO_2: 2Eu^{3+}: 1.2Yb^{3+} : x Er^{3+} (x = 0.1. 1.0. 3.0 and 7.0 mol% heat-treated at 700. 800. 900 and 1000 °C prepared by the sol-gel process.

Width of the band assign to $^5D_0 \rightarrow {}^7F_0$ of the samples based on $30Si^{4+}$ - $70Ti^{4+}$								
Temp. (°C)	0.1 mol% of Er^{3+}		1.0 mol% of Er^{3+}		3.0 mol% of Er^{3+}		7.0 mol% of Er^{3+}	
	Excitation wavelength							
	394	463	394	463	394	463	394	463
700	4.95	5.33	6.07	6.33	5.48	5.78	7.56	6.65
800	5.81	6.14	5.62	6.39	–	6.83	–	–
900	6.88	5.93	–	6.49	–	6.40	–	7.04
1000	6.64	5.52	–	6.19	–	5.89	–	6.04
Width of the band assign to $^5D_0 \rightarrow {}^7F_0$ of the samples based on $70Si^{4+}$ - $30Ti^{4+}$								
Temp. (°C)	0.1 mol% of Er^{3+}		1.0 mol% of Er^{3+}		3.0 mol% of Er^{3+}		7.0 mol% of Er^{3+}	
	Excitation wavelength (nm)							
	394	463	394	463	394	463	394	463
700	5.92	5.74	7.13	5.62	5.90	6.14	–	–
800	6.46	6.57	6.82	6.04	8.03	6.54	–	–
900	–	7.59	9.71	7.06	–	–	–	–
1000	–	6.88	10.43	7.07	–	7.41	–	–

–: It was not possible to determine.

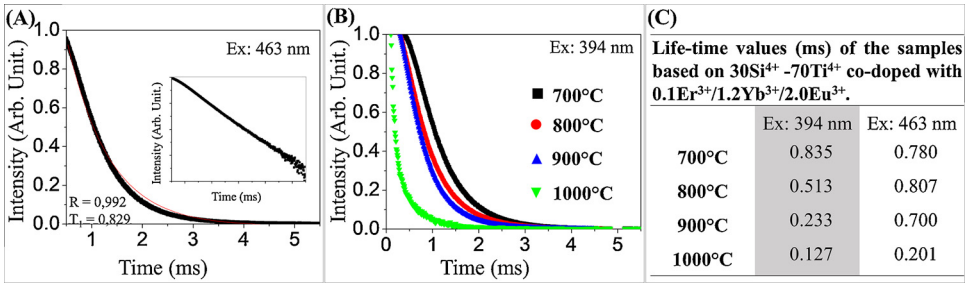

(C)

Life-time values (ms) of the samples based on $30Si^{4+}$ -$70Ti^{4+}$ co-doped with $0.1Er^{3+}/1.2Yb^{3+}/2.0Eu^{3+}$.

	Ex: 394 nm	Ex: 463 nm
700°C	0.835	0.780
800°C	0.513	0.807
900°C	0.233	0.700
1000°C	0.127	0.201

Fig. 4. Decay curve of the samples based on $30Si^{4+}$ -$70Ti^{4+}$ co-doped with 0.1 mol% of Er^{3+}/1.2 mol% of Yb^{3+}/2.0 mol% of Eu^{3+} (A) heat-treated at 700 °C, adjusted an exponential decay of 1 st order, under excitation at 394 nm. (B) Heat-treated at different temperatures. (C) Life time values (ms) of the samples fixing the excitation at 394 nm or 463 nm.

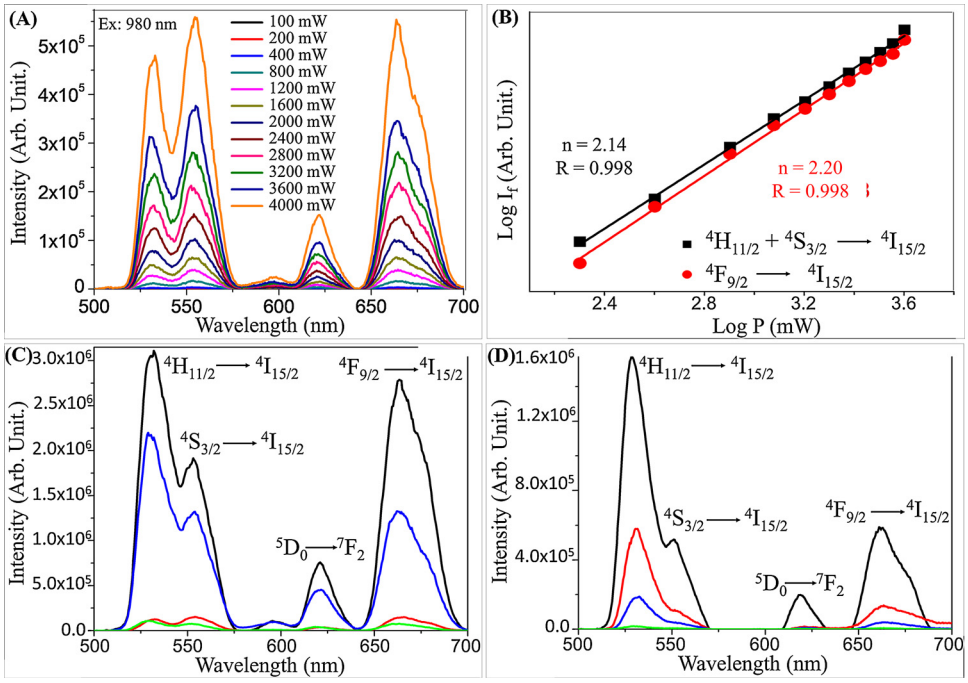

Fig. 5. Spectra obtained by Up conversion phenomenon. (A) Emission spectra of the samples based on $30Si^{4+}$-$70Ti^{4+}$ co-doped with 0.1 mol% of Er^{3+}/1.2 mol% of Yb^{3+}/2.0 mol% of Eu^{3+} heat-treated at 800 °C excited with a 980 nm pumping laser and power ranging from 200 mW to 4000 mW. (B) Log graph of photoluminescence intensity by laser power log of the samples based on $30Si^{4+}$-$70Ti^{4+}$ co-doped with 0.1 mol% of Er^{3+}/1.2 mol% of Yb^{3+}/2.0 mol% of Eu^{3+} heat-treated at 800 °C. (C) Emission spectra of the samples based on $30Si^{4+}$-$70Ti^{4+}$ co-doped with 0.1 mol% of Er^{3+}/1.2 mol% of Yb^{3+}/2.0 mol% of Eu^{3+} treated at different temperatures with a 980 nm pumping laser and power ranging of 2400 mW. (D) Emission spectra of the samples based on $70Si^{4+}$-$30Ti^{4+}$ co-doped with 0.1 mol% of Er^{3+}/1.2 mol% of Yb^{3+}/2.0 mol% of Eu^{3+} treated at different temperatures with a 980 nm pumping laser and power ranging of 2400 mW.

Table 6
Number of photons involved on the excitation mechanism of up conversion of the samples based on SiO_2-TiO_2: 2.0 mol% of Eu^{3+}: 1.2 mol% of Yb^{3+}: x mol% of Er^{3+} (x = 0.1. 1.0. 3.0 and 7.0 mol% heat-treated at 700. 800. 900 and 1000 °C prepared by the sol-gel process.

Number of photons involved on the excitation mechanism of Upconversion for the samples based on $30Si^{4+}$ - $70Ti^{4}$

Temp. (°C)	Transitions	0.1 mol% of Er^{3+}	1.0 mol% of Er^{3+}	3.0 mol% of Er^{3+}	7.0 mol% of Er^{3+}
700	$^2H_{11/2}+{}^4S_{3/2}\rightarrow 4I_{15/2}$	**2.03**	**1.87**	**1.89**	**1.68**
	$^4F_{9/2}\rightarrow {}^4I_{15/2}$	1.91	1.90	1.98	1.85
800	$^2H_{11/2}+{}^4S_{3/2}\rightarrow 4I_{15/2}$	**2.14**	**1.96**	**1.76**	**1.59**
	$^4F_{9/2}\rightarrow {}^4I_{15/2}$	2.20	1.79	1.79	1.68
900	$^2H_{11/2}+{}^4S_{3/2}\rightarrow 4I_{15/2}$	**2.22**	**1.94**	**1.83**	**1.61**
	$^4F_{9/2}\rightarrow {}^4I_{15/2}$	2.04	1.84	1.71	1.55
1000	$^2H_{11/2}+{}^4S_{3/2}\rightarrow 4I_{15/2}$	**2.32**	**1.77**	**1.69**	**1.58**
	$^4F_{9/2}\rightarrow {}^4I_{15/2}$	2.21	1.71	1.70	1.62

Number of photons involved on the excitation mechanism of Upconversion for the samples based on $70Si^{4+}$ - $30Ti^{4}$

Temp. (°C)	Transitions	0.1 mol% of Er^{3+}	1.0 mol% of Er^{3+}	3.0 mol% of Er^{3+}	7.0 mol% of Er^{3+}
700	$^2H_{11/2}+{}^4S_{3/2}\rightarrow 4I_{15/2}$	**2.33**	**2.24**	**1.99**	**1.80**
	$^4F_{9/2}\rightarrow {}^4I_{15/2}$	1.88	2.06	2.07	2.26
800	$^2H_{11/2}+{}^4S_{3/2}\rightarrow 4I_{15/2}$	**2.49**	**2.05**	**1.97**	**1.79**
	$^4F_{9/2}\rightarrow {}^4I_{15/2}$	1.99	2.12	1.80	2.26
900	$^2H_{11/2}+{}^4S_{3/2}\rightarrow 4I_{15/2}$	**2.42**	**2.00**	**1.82**	**1.71**
	$^4F_{9/2}\rightarrow {}^4I_{15/2}$	2.02	2.00	2.53	1.80
1000	$^2H_{11/2}+{}^4S_{3/2}\rightarrow 4I_{15/2}$	**2.45**	–	**1.89**	**1.71**
	$^4F_{9/2}\rightarrow {}^4I_{15/2}$	2.59	–	1.93	2.27

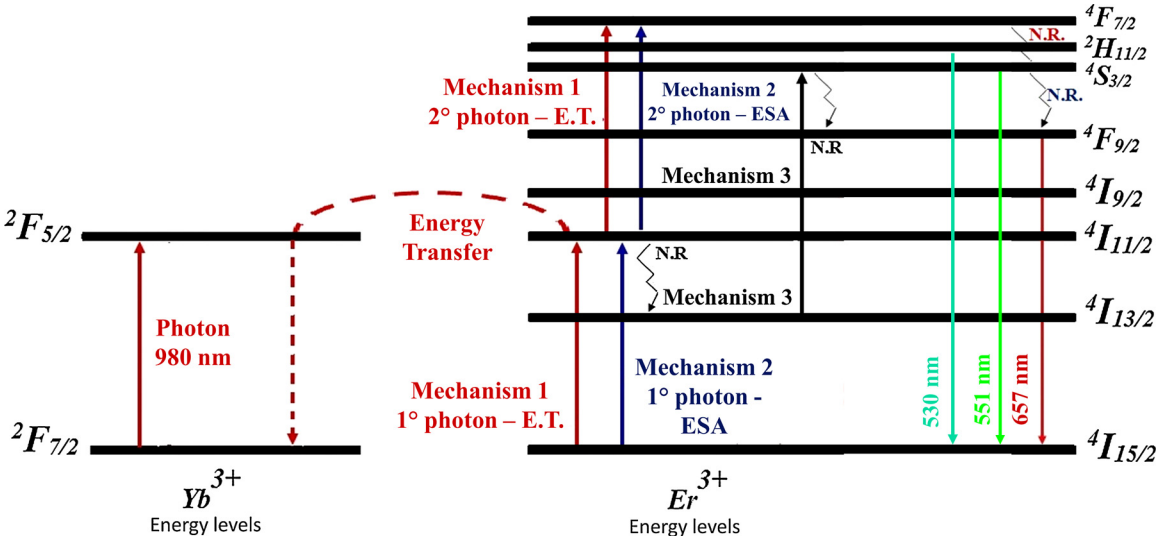

Fig. 6. Possible mechanisms of up conversion.

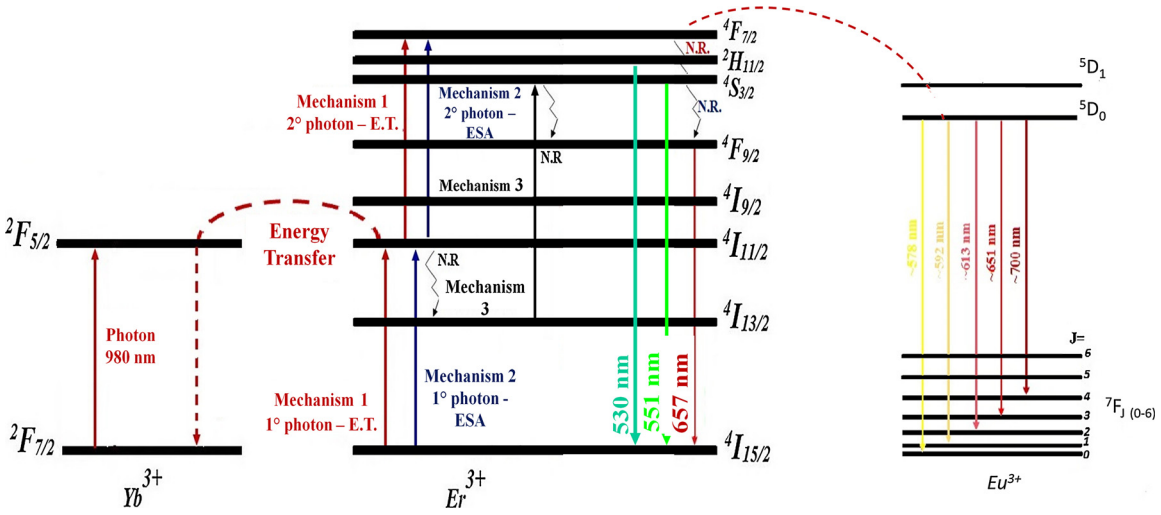

Fig. 7. Possible mechanism of energy transfer between Er^{3+} and Eu^{3+}.

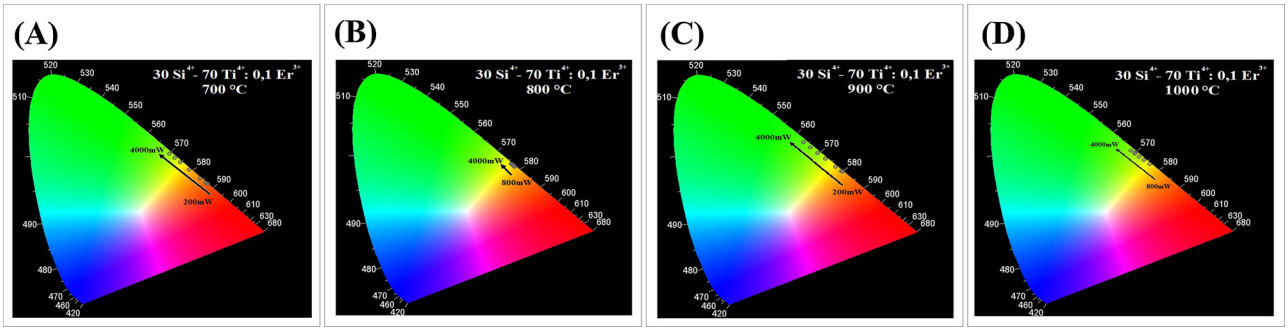

Fig. 8. Diagram of chromaticity of the sample based on $30Si^{4+}$-$70Ti^{4+}$ co-doped with $0.1Er^{3+}/1.2Yb^{3+}/2.0Eu^{3+}$ and treated at different temperatures under excitation with a 980 nm pumping laser.

the same time. In these samples, the behavior of the emission at red region (between 600–640 nm) depends on the excitation wavelength, the temperature of heat treatment, and the percentage of dopants.

Comparing the samples that underwent simple (394 nm) or double (394 and 980 nm) excitation, there is a small reduction in the red emission for the samples treated at 700 and 800 °C when using a dual beam. At higher temperatures, it promotes a slight increase. However, the inverse occurs when the excitation sources used were 463 nm and a double beam (463 and 980 nm) – the red emission area growths with the double excitation just for the samples treated at 700 and 800 °C. The double excitation interferes with the red emission since the absorption of two photons by Er^{3+} can promote an energy transfer between Er^{3+} and Eu^{3+} states and the subsequent emission in the red region. However, in general, the double excitation promotes an increase of the photoluminescence.

The potential of these materials for applications in

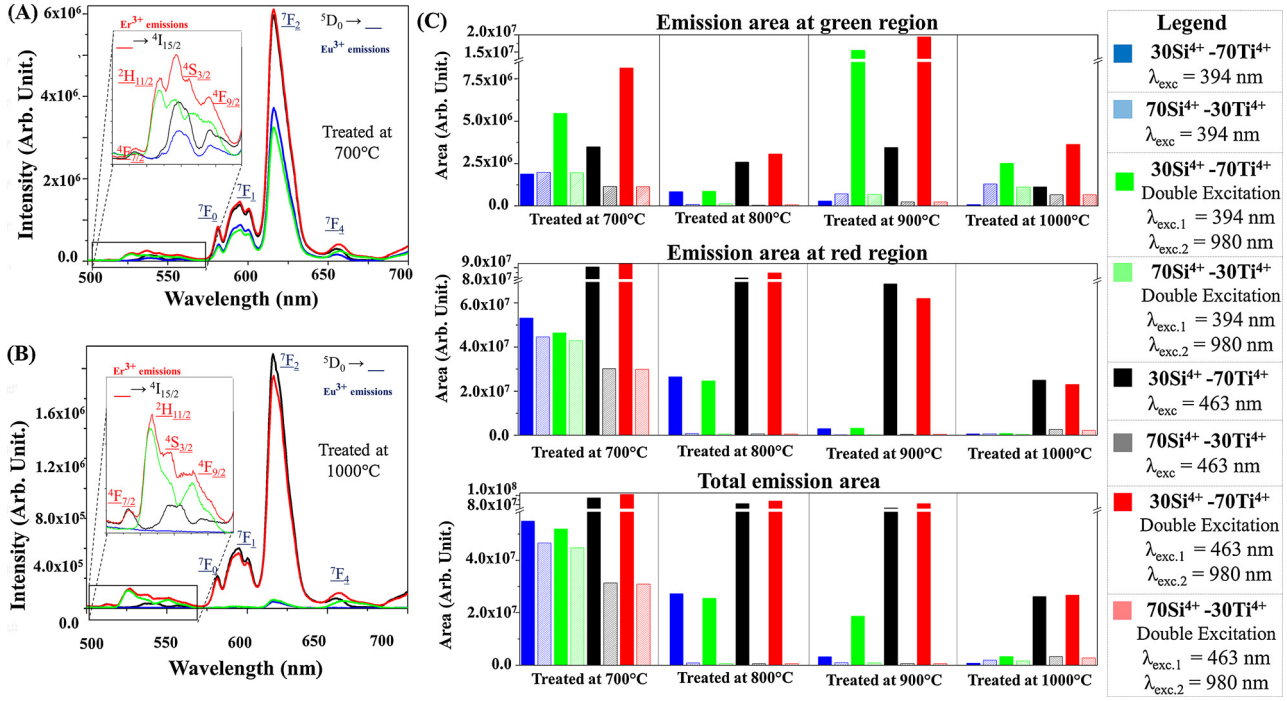

Fig. 9. Emission spectra varying the excitation wavelengths. (A) Samples based on $30Si^{4+}$-$70Ti^{4+}$ co-doped with 0.1 mol% of Er^{3+}/1.2 mol% of Yb^{3+}/2.0 mol% of Eu^{3+} treated on 700 °C. (B) Samples based on $30Si^{4+}$-$70Ti^{4+}$: 0.1 mol% of Er^{3+}/1.2 mol% of Yb^{3+}/2.0 mol% of Eu^{3+} treated on 1000 °C. (C) Histograms of the emission areas on the red/green regions of the electromagnetic spectrum and the sum between these areas, of the samples based on $30Si^{4+}$-$70Ti^{4+}$ and $70Si^{4+}$-$30Ti^{4+}$ co-doped with 0.1 mol% of Er^{3+}/1.2 mol% of Yb^{3+}/2.0 mol% of Eu^{3+} treated in different temperatures (For interpretation of the references to colour in this figure legend, the reader is referred to the web version of this article).

telecommunications devices were confirmed by the analysis of the IR emissions, as shown in Fig. 10. All the samples showed a large emission band at 1450–1700 nm. It is due to the $^4I_{13/2} \rightarrow {}^4I_{15/2}$ transition of Er^{3+} states [12]. This emission can occur though two mechanisms. The first mechanism is due to the energy absorption by the Er^{3+}, promoting their electrons to the $^4I_{11/2}$ state. Part of this energy is lost by non-radiative processes and the IR emission occurs when the electrons populate the $^4I_{13/2}$ state. Another mechanism, more efficient, happens through the energy transfer between the Yb^{3+} and Er^{3+} ions. A 980 nm photon is absorbed by Yb^{3+}, promoting the electrons to the excited state $^2F_{5/2}$, when this energy is emitted by Yb^{3+}, it is immediately re-absorbed by the Er^{3+}, causing the subsequent emission.

The intensity of the emission is proportional to the laser power and it is possible to observe it even when using low laser power, as shown in Fig. 10(A). The samples treated at 800 and 900 °C exhibit the most intense and extended spectra – Fig. 10(B). The increase of the annealing temperature favors a decrease in the defects and suppressors groups of the photoluminescence. Especially on the infrared Er^{3+} emission, the presence of −OH groups is extremely prejudicial. The stretch energy of two groups −OH is around 3255 cm^{-1}, the same energy emitted by Er^{3+}. Despite this, there is a significant reduction in the emission intensity for the materials treated at 1000 °C. The incorporation of RE^{3+} in the TiO_2 is difficult and their presence on the surface of the material promotes loss by phonons.

Fig. 10 exhibits the full width at half emission maximum. The sample treated at 800 °C presents an extremely broad emission. It occurs due the presence of RE^{3+} in several sites of symmetry. This is confirmed though the asymmetric ratio, shown in Table 4. Their ratio was the largest.

With the exception of the sample doped with 0.1 mol % of Er^{3+}, increasing the dopant percentage, the emissions become weaker, due to the cross relation, but they widen. When the concentration of RE^{3+} is high, their incorporation in the crystalline structure is more difficult, promoting their presence in the vacancies and on the surface of the material, this causes the enlargement of the emissions due to the presence of RE^{3+} in different sites of symmetry.

4. Conclusion

Based on the results, it is possible to obtain materials based on SiO_2-TiO_2 co-doped with Er^{3+}/Yb^{3+}/Eu^{3+} by the sol-gel process that present photo luminescent properties of both downconversion and up conversion. They are able to absorb UV and IR energy and emit in the visible region, permitting the dye re-absorb ions at this energy. Thus, they have potential for application in solar cells, as they can be used for the strategy to use the solar spectrum, improving the solar cell efficiency. The doping of the materials promotes a decrease of their band gap. Their crystalline phase depends on the heat treatment temperature. The rutile is extremely harmful to the photoluminescence due to their center of inversion. Despite the brookite phase being the least symmetrical, it has the highest packing density, making the incorporation of the RE^{3+} in the TiO_2 difficult. Lastly, the preferential crystalline phase of the materials is anatase. It presented the highest photocatalytic activity, the highest refractive index avoiding loses by reflection, the smallest sizes increasing the surface area of the materials, the lowest packing density facilitating the incorporation of the RE^{3+} on the TiO_2 and the highest emission intensity promoting a better re-absorption by the dye. Based on this, the best temperature of heat treatment is 700 °C. The binary systems stabilize the metastable phases, permitting them to appear at higher temperatures. It favors the elimination of defects and suppressor groups of the photoluminescence. However, the matrix containing a greater amount of Ti^{4+} is preferable. The better percentage of dopant is 0.1 mol% of Er^{3+}. Increasing this concentration brings losses by non-radiative processes. In conclusion, the best synthesis conditions to obtain materials with potential to improve the solar cells efficiency could be determined.

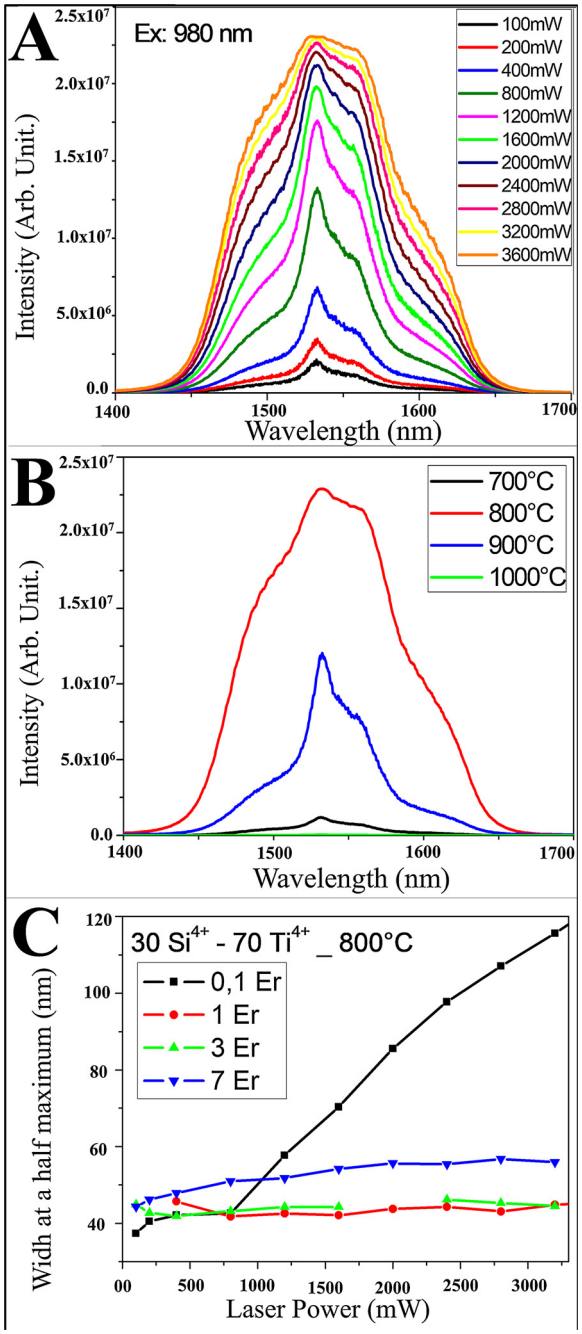

Fig. 10. IR emission spectra with 980 nm pumping laser excitation of the samples based on $30Si^{4+}$-$70Ti^{4+}$ co-doped with 0.1 mol% of Er^{3+}/1.2 mol% of Yb^{3+}/2.0 mol% of Eu^{3+}. (A) Heat-treated at 800 °C and power ranging from 100 to 3600 mW. (B) Fixing the laser power in 3200 mW and varying the annealing temperature. (C) Fixing the laser power in 3200 mW and the annealing temperature in 800 °C and varying the RE^{3+} percentage.

Acknowledgments

This work was supported by FAPEMIG, CAPES, CNPq and FINEP. This work is a collaboration research project of members of the Rede Mineira de Química (RQ-MG) supported by FAPEMIG (Project: CEX - RED-00010-14).

References

[1] M. Baraton, Nano-TiO_2 for solar cells and photocatalytic water splitting scientific and technological challenges for commercialization, Open Nanosci. J. 5 (2011) 66–77.
[2] J.Z. Chen, H.C. Yu, W.D. Sincoskie, Meeting the broadband access infrastructure demands: the promise of gigabit ethernet, Technol. Forecast. Soc. Change 72 (2005) 1–10.
[3] D.H.S. Reis, J.M.M. Buarque, M.A. Schiavon, E. Pecoraro, S.J.L. Ribeiro, J.L. Ferrari, Simples and cost-effective method to obtain RE^{3+}-doped Al_2O_3 for possible photonic applications, Ceram. Int. (2015) 1–8.
[4] A. Yella, H.W. Lee, H.N. Tsao, C. Yi, A.K. Chandiran, M.K. Nazeeruddin, E.W.G. Diau, C.Y. Yeg, S.M. Zakeeruddin, M. Grätzel, Phophyrin-sensitizer solar cells with cobalt (II-III)-based redox electrolyte exceeds 12 percent efficiency, Science 334 (201) (2018) 629–634.
[5] M. Que, W. Que, X. Yin, J. Shao, Enhanced sunlight harvesting of dye-sensitized solar cells through the insertion of a (Sr, Ba, Eu)$_2SiO_4$-TiO_2 composite layer, Mater. Res. Bull. 83 (2016) 19–23.
[6] S. Ito, T.N. Murakami, P. Comte, P. Liska, C. Grätzel, M.K. Nezeeruddin, M. Grätzel, Fabrication of thin films dry sensitizer solar cells with solat to electric power conversion efficiency over 10%, Thin Solid Films 516 (2008) 4613–4619.
[7] S. Saehna, R. Prasetyowati, M.I. Hidayat, P. Arifin, M.K. Abdullah, Efficiency improvement in TiO_2-particle base solar cells after deposition of metal in spaces between particles, Int. J. Basic Appl. Sci. 11 (2011) 15–28.
[8] M.R. Mohammadi, A.M. Bakhshayesh, Improved efficiency of dye-sensitized solar cells by design of a proper double layer photo anode electrodes composed of Cr-doped TiO_2 transparent and light scattering layer, J. Solgel Technol. 67 (2013) 77–87.
[9] R. Su, R. Bechstein, J. Kibsgaard, R.T. Vang, F. Besenbacher, High-quality Fe-doped TiO_2 with superior visible-light performance, J. Mater. Chem. 22 (2012) 23755–23758.
[10] D.H. Kim, K.S. Lee, Y.S. Kim, Y.C. Chung, S.J. Kim, Photocatalytic activity of Ni 8 wt %-doped TiO_2 photocatalyst synthesized by mechanical alloying under visible light, J. Am. Ceram. Soc. 89 (2006) 515–518.
[11] G.R. Deng, X.H. Xia, M.L. Guo, Y. Gao, G. Shao, Mn-doped TiO_2 nano powders with remarkable visible light photocatalytic activity, Mater. Lett. 65 (2011) 2051–2054.
[12] L.A. Rocha, A.C. Pereira, M.A. Schiavon, J.L. Ferrari, Up conversion and infrared emission of Er^{3+}/Yb^{3+} co-doped SiO_2-Gd_2O_3 obtained by sol-gel process, Process. Appl. Ceram. 9 (2015) 23–31.
[13] A. Apostoluk, Y. Zhu, B. Canut, B. Masenelli, J. Delaunay, K. Znajdek, M. Sibinski, Investigation of luminescent properties of ZnO nanoparticles for their use as a down-shifting layers on solar cells, Multiple J. Found 10 (2013) 1301–1307.
[14] L.G.A. Carvalho, L.A. Rocha, J.M.M. Buarque, R.R. Gonçalves, C.S. Nascimento Jr, M.A. Schiavon, S.J.L. Ribeiro, J.L. Ferrari, Color tunability in green, red and infrared up conversion emission in Tm^{3+} /Yb^{3+}/Ho^{3+} co-doped CeO_2 with potential application for improvement of efficiency in solar cells, J. Lumin. 159 (2015) 223–228.
[15] L. Zhlong, Y. Yuming, Y. Chun, Luminescent properties of co-doping Y_2O_3:Eu^{3+}, Me (Me = Mg^{2+}, Ca^{2+}) nanohods, J. Nanopart. 12 (2010) 2233–2240.
[16] C.K. Huang, Y.C. chen, W.B. Hung, T.M. Chen, K.W. Sun, W.L. Chang, Enhanced light harvesting of Si solar cells via luminescent down-shifting using YVO_4:Bi^{3+},Eu^{3+} nanophosphors, Prog. Photovolt. Res. Appl. 21 (2013) 1507–1513.
[17] O.L. Malta, S.J.L. Ribeiro, M. Faucher, P. Porcher, Theoretical intensities of 4f-4f transitions between stark levels of the Eu^{3+} ion in crystal, J. Phys. Chem. Solids 52 (1991) 587–593.
[18] Y. Chang, H. Lin, Y. Chai, Y. Li, Preparation and luminescent properties of europium-activated $YinGe_2O_7$ phosphors, J. Alloy Comp. 460 (2008) 421–425.
[19] Caldiño U, E. Alvarez, A. Speguini, M. Bettinelli, New greenish-yellow and yellowish-green emitting glass phosphors: Tb^{3+}/Eu^{3+} and $Ce^{3+}/Tb^{3+}/Eu^{3+}$ in zinc phosphate glasses, J. Lumin. 135 (2013) 216–220.
[20] J. Wild, A. Meijerink, J.K. Rath, W.G.J.H.M.V. Stark, R.E.I. Schropp, Upconverter solar cells: materials and applications, Energy Environ. Sci. 4 (2011) 4835–4848.
[21] C. Ronda, A. Srivastava, Luminescent Science and Display Materials, The Electrochemical Society Interface, Springer, 2006, pp. 55–57.
[22] R.R. Gonçalves, G. Carturan, M. Montagna, M. Ferrari, L. Zampedri, S. Pelli, G.C. Righini, S.J.L. Ribeiro, Y. Messadeq, Erbium-actived HfO_2-based waveguides for photonics, Opt. Mater. 25 (2004) 131–139.
[23] H.Q. Liu, L.L. Wang, S. Chen, Effect of Yb^{3+} concentration on the upconversion of Er^{3+} ion doped La_2O_3 nanocrystals under 980 nm excitation, Mater. Lett. 61 (2007) 3629–3631.
[24] X. Orignac, D. Barbier, X.M. Du, R.M. Almeida, O. Mccarthy, E. Yeatman, Sol-gel silica/titânia-on-silicon Er/Yb-doped waveguides for optical amplification at 1.5mm, Opt. Mater. 12 (1999) 1–18.
[25] L.A. Rocha, M.A. Schiavon, S.J. Ribeiro, R.R. Gonçalves, J.L. Ferrari, Eu^{3+}-doped SiO_2-GdO_2 prepared by the sol-gel process: structural and optical properties, J. Solgel Sci. Technol. 76 (2015) 260–270.
[26] O. Berkani, K. Latrous, H. Hamzaoui el, B. Capoen, M. Bouazaoui, Effects of heat treatment and TiO_2 content on the optical properties of Eu^{3+} doped TiO_2-SiO_2 thin films, J. Lumin. 113 (2012) 2979–2983.
[27] I.M. Azzouz, L.C. Klein, Red, violet and upconversion luminescence of Eu/Sm co-doped sol gel SiO_2-TiO_2, Opt. Mater. 35 (2012) 292–296.
[28] C.M. Wahang, C.S. Yeo, Y.H. Kim, Preparation and characterization of sol-gel derived SiO_2-TiO_2-PDMS composite films, Bull. Korean Chem. Soc. 22 (2001) 1366–1370.
[29] S. Yi, J.S. Bae, B.K. Moon, J.H. Jeong, J.H. Kim, Highly enhanced luminescence of monocrystalline TiO_2:Eu^{3+} phosphors, Opt. Mater. 28 (2006) 610–614.
[30] X. Wang, G. Wu, B. Zhou, J. Shen, Thermal annealing effect on optical properties of binary TiO_2-SiO_2 sol-gel coatings, Materials 6 (2013) 76–84.
[31] K.K. Saini, S.D. Sharma, M.K. Chanderkant, D. Singh, C.P. Sharma, Structural and optical properties of TiO_2 thin films derived by sol-gel dip coating process, J. Non-

Cryst. Solids 353 (2007) 2469–2473.
[32] R.M. Mohamed, I.A. Mkhalid, The effect of rare earth dopants on the structure, surface, texture and photocatalytic properties of TiO_2-SiO_2 prepared by sol-gel method, J. Alloy 501 (2010) 143–147.
[33] J.L. Ferrari, K.O. Lima, E. Pecoraro, R.A.S. Ferreira, R.R. Gonçalves, Color tunability of intense upconversion emission from Er^{3+}-Yb^{3+} co-doped SiO_2-Ta_2O_5 glass ceramic planar waveguides, J. Mater. Chem. 22 (2012) 9901–9908.
[34] Y. Hu, H.L. Tsai, C.L. Huang, Effect of brookite phase on the anatase-rutile transition in titania nanoparticles, J. Eur. Ceram. Soc. 23 (2003) 691–696.
[35] M. Pal, U. Pal, J.M.G.Y. Jiménez, F.P. Rodríguez, Effects of crystallization and dopant concentration on the emission behavior TiO_2:Eu nanophosphors, Nanoscale Res. Lett. 7 (2012) 1–12.
[36] M.N. Iliev, V.G. Hadjiev, A.P. Litvinchuk, Raman and infrared spectra of brookite (TiO_2): experiment and theory, Vib. Spectrosc. 64 (2013) 148–152.
[37] W. Hu, L. Li, G. Li, C. Tang, L. Sun, High-quality brookite TiO_2 flowers: synthesis, characterization and dielectric performance, Cryst. Growth Desing. 9 (2009) 3676–3682.
[38] A.R. Zanatta, A fast reliable methodology to estimate the concentration of rutile or anatase phases of TiO_2, AIP Adv. 7 (2017) 075201-1 – 075201-7.
[39] C.H. Kwon, J.H. Kim, I.S. Jung, H. Shin, K.H. Yoon, Preparation and characterization of TiO_2-SiO_2 nano-composite thin films, Ceram. Int. 29 (2003) 851–856.
[40] F.T. Aquino, J.L. Ferrari, S.J.L. Ribeiro, A. Ferrier, P. Goldner, R.R. Gonçalves, Broadband NIR emission in novel sol-gel Er^{3+}-doped SiO_2-Nb_2O_5 glass ceramic planar waveguides for photonic applications, Opt. Mater. 35 (2012) 387–396.
[41] O.L. Malta, S.J.L. Ribeiro, M. Faucher, P. Porcher, Theoretical intensities of 4f-4f transitions between stark levels of the Eu^{3+} ion in crystal, J. Phys. Chem. Solids 52 (1991) 587–593.
[42] J.H. Leal, Y. Cantu, D.F. Gonzalez, J.G. Parson, Brokite and anatase nanomaterial polymorphs of TiO_2 synthesized from $TiCl_3$, Inorg. Chem. Commun. 84 (2017) 28–32.
[43] X. Wang, Ql. Bu, A. Yanyan, C. Liu, Optical temperature sensing of rare-earth ions doped phosphors, RSC Adv. 5 (2015) 86219–86236.
[44] M. Ferhi, K. Horchani-Naifer, M. Férid, Combustion synthesis and luminescence properties of $LaPO_4$:Eu^{3+} (5%), J. Rare Earth 27 (2009) 182–186.
[45] V.G. Pol, J.M. Calderon-moreno, Fabrication of luminescent Eu_2O_3 superstructures, Phys. Chem. Lett. 1 (2010) 319–322.
[46] Y. Gao, J. Gong, M. Fan, Q. Fang, N. Wang, W. Han, Z. Xu, Large-scale synthesis of Lu_2O_3:Ln^{3+} (Ln^{3+} = Eu^{3+}, Tb^{3+}, $Yb^{3+}Er^{3+}$, $Yb^{3+}Tm^{3+}$, Yb^{3+}/Ho^{3+}) microspheres and their photoluminescence properties, Mater. Res. Bull. 47 (2012) 4135–4137.
[47] W. Jia, H. Liu, S.P. Felofilov, R. Meltzer, J. Jiao, Spectroscopy study of Eu^{3+}, Y^{3+} -codoped SiO_2 sol gel glasses, J. Alloy 303 (2000) 336–339.
[48] M. Mohapatra, V. Natarajan, S.V. Godbole, Speciation of Eu^{3+} in sol-gel derived alkali barium borosilicate glasses: time resolved photoluminescence (TRPL) and judd-ofelt analysis, J. Non-Cryst. Solids 386 (2014) 115–120.
[49] I. Zareba-Grodz, R. Pazik, W. Tylus, W. Mielcarek, K. Hermanowicz, W. Strek, K. Maruszewski, Europium-doped silica-titania thin films obtained by sol-gel method, Opt. Mater. 29 (2007) 1103–1106.
[50] G. Alombert-Goget, N. Gaumer, J. Obriot, A. Rammal, S. Chaussedent, A. Monteil, H. Portales, A. Chiasera, M. Ferrari, Aluminum effect on photoluminescence properties of sol-gel-derived Eu^{3+}-activated silicate glasses, J. Noncryst. Solids 351 (2005) 1754–1758.
[51] B.K. Moon, I. Know, H.K. Yang, H.J. Seo, J.H. Jeong, S.S. Yi, J.H. Kim, Spectroscopy of nanocrystalline TiO_2:Eu^{3+} phosphors, Colloids Surf. 331 (2008) 82–86.
[52] Y. Wu, H. Suo, D. He, C. Guo, Highly sensitive up-conversion optical thermometry based on Yb^{3+}-Er^{3+} co-doped $NaLa(MoO_4)_2$ green phosphors, Mater. Res. Bull. (2018).
[53] S.K. Ranjan, M. Mondal, V.K. Rai, Er^{3+}-Yb^{3+}/ Er^{3+}-Yb^{3+}-Li^{+}/ Er^{3+}-Yb^{3+}-Zn^{2+}:Gd_2O_3 nanophosphors for efficient frequency upconverter and temperature sensing applications, Mater. Res. Bull. (2018).